ADVANCED MATERIALS
www.advmat.de

An Integrated Deposition and Passivation Strategy for Controlled Crystallization of 2D/3D Halide Perovskite Films

Tim Kodalle, Mahdi Malekshahi Byranvand, Meredith Goudreau, Chittaranjan Das, Rajarshi Roy, Małgorzata Kot, Simon Briesenick, Mohammadreza Zohdi, Monika Rai, Nobumichi Tamura, Jan Ingo Flege, Wolfram Hempel, Carolin M. Sutter-Fella,* and Michael Saliba**

This work introduces a simplified deposition procedure for multidimensional (2D/3D) perovskite thin films, integrating a phenethylammonium chloride (PEACl)-treatment into the antisolvent step when forming the 3D perovskite. This simultaneous deposition and passivation strategy reduces the number of synthesis steps while simultaneously stabilizing the halide perovskite film and improving the photovoltaic performance of resulting solar cell devices to 20.8%. Using a combination of multimodal in situ and additional ex situ characterizations, it is demonstrated that the introduction of PEACl during the perovskite film formation slows down the crystal growth process, which leads to a larger average grain size and narrower grain size distribution, thus reducing carrier recombination at grain boundaries and improving the device's performance and stability. The data suggests that during annealing of the wet film, the PEACl diffuses to the surface of the film, forming hydrophobic (quasi-)2D structures that protect the bulk of the perovskite film from humidity-induced degradation.

1. Introduction

Hybrid metal halide perovskites have garnered significant interest in recent years due to their impressive optical and electrical properties, as well as their compositional variability and facile processing pathways.[1–3] However, despite their potential for high-efficiency solar cells, perovskite thin films are prone to degrade in ambient environments, especially in humid air.[2,4] The community is investigating several approaches to overcome these stability issues and achieve higher efficiencies, for example the use of NiO_x interlayers,[5–8] additives,[9,10] or encapsulation strategies.[11,12] Another effective approach for improving the stability of perovskite films is by intercalating large, bulky organic molecules into the surface area of

T. Kodalle, M. Goudreau, S. Briesenick, C. M. Sutter-Fella
Molecular Foundry
Lawrence Berkeley National Laboratory
1 Cyclotron Road, Berkeley, California 94720, USA
E-mail: csutterfella@lbl.gov

T. Kodalle, N. Tamura
Advanced Light Source
Lawrence Berkeley National Laboratory
1 Cyclotron Road, Berkeley, California 94720, USA

M. M. Byranvand, C. Das, R. Roy, M. Zohdi, M. Rai, M. Saliba
Institute for Photovoltaics
University of Stuttgart
Pfaffenwaldring 47, 70569 Stuttgart, Germany
E-mail: mahdi.malekshahi@ipv.uni-stuttgart.de; michael.saliba@ipv.uni-stuttgart.de

The ORCID identification number(s) for the author(s) of this article can be found under https://doi.org/10.1002/adma.202309154

DOI: 10.1002/adma.202309154

M. M. Byranvand, C. Das, M. Saliba
Helmholtz Young Investigator Group FRONTRUNNER
IEK5-Photovoltaik
Forschungszentrum Jülich
52425 Jülich, Germany

M. Kot, J. I. Flege
Chair of Applied Physics and Semiconductor Spectroscopy
Brandenburg University of Technology Cottbus-Senftenberg
03046 Cottbus, Germany

S. Briesenick
Department of Physics, Ernest Rutherford Physics Building
McGill University
3600 Rue University, Montrèal QC H3A 2T8, Canada

W. Hempel
Zentrum für Sonnenenergie- und Wasserstoff-Forschung
Baden-Württemberg (ZSW)
70563 Stuttgart, Germany

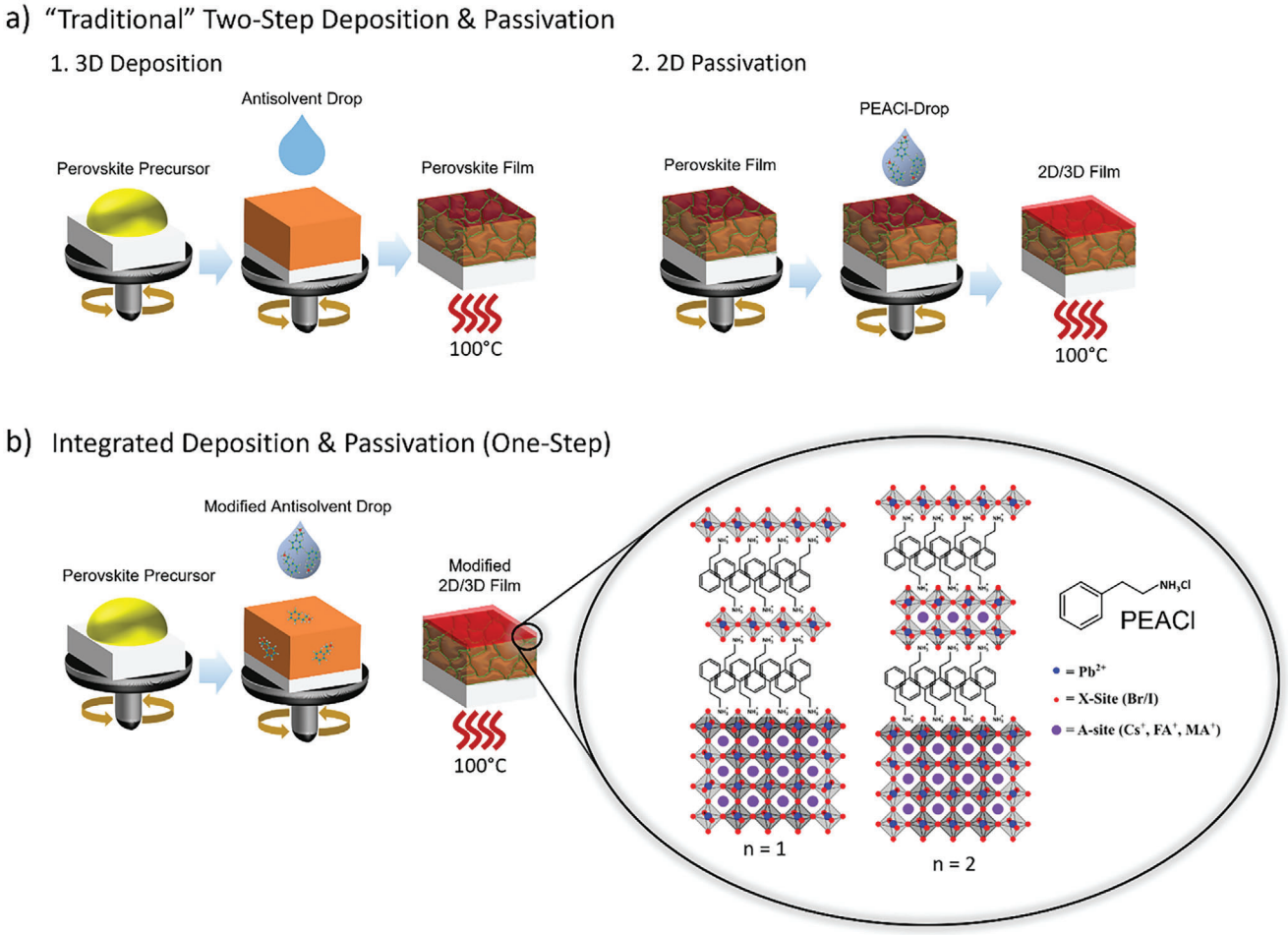

Figure 1. Schematic comparing the "traditional" deposition and passivation processes (top row) and the integrated deposition and passivation strategy to form 2D passivated 3D halide perovskite films (bottom row). a) With the traditional procedure, the 3D perovskite is first deposited using antisolvent-assisted spin coating and subsequent annealing. Then, in a second step, the completed perovskite film is spin-coated again to deposit a bulky molecule, that is, PEACl in IPA, before annealing a second time. b) Using the integrated deposition and passivation strategy, the PEACl is added to the antisolvent and deposited onto the rotating wet film during the first (and only) spin coating process. The mixed 2D/3D film is then annealed on a hotplate. The inset in the bottom right illustrates the crystal structure of a 2D/3D ($n = 1$) and a quasi-2D/3D ($n > 1$) film.

the thin films.[13–17] Some of the commonly used molecules are phenethyl ammonium halides such as PEAI, PEABr, and PEACl, thiophene methylammonium halides such as TMAI, TMABr, and TMACl and others.[18,19] Interestingly, there seems to be a trend that higher performing perovskite solar cells can be achieved when using heavier halides.[18,19] The typical synthesis involves the deposition of organic molecules onto prefabricated 3D halide perovskite films. Exposing the surface of the perovskite thin film to these bulky molecules leads to 2D or quasi-2D structures at the surface of the 3D film. During this process, these hydrophilic molecules intercalate between the octahedra of the perovskite crystal, creating (quasi-)2D slabs that protect the bulk perovskite from humidity-induced degradation (see **Figure 1**). Additionally, it has been reported that the (quasi-)2D structures passivate point defects at the perovskite surface, creating a tunneling junction with reduced interface recombination and therefore increasing the power conversion efficiency (*PCE*) of the resulting solar cells.[13,20] Typically, these 2D/3D structures are fabricated in a two-step process (Figure 1a). First, the bulk 3D perovskite layer is deposited by, for example, an antisolvent-assisted spin coating procedure followed by thermal annealing. The complete film is cooled down to room temperature and then, in a second step, the bulky molecules are deposited using spin coating and a second annealing step.[14,21,22] Other approaches include the evaporation of the bulky molecules onto the completed perovskite film.[23] In either case, the deposition of the molecules on top of the thin-film leads to intercalation solely at the surface of the already finished 3D perovskite film and therefore formation of the (quasi-)2D structures only at the surface.[24] Several groups have shown that these procedures can lead to significant improvements in device efficiency and stability using a variety of different bulky molecules with optimized process conditions. However, the need for a second deposition step increases process complexity and duration, and therefore material and energy consumption of the fabrication process. To simplify the deposition and fabrication

steps, recently, some groups have reported processes for 2D/3D formation by combining the deposition of bulky iodide-based molecules with the dripping of the antisolvent.[25,26] Both studies showed that integration of bulky molecules into the antisolvent can be an effective way to improve efficiency and stability of perovskite-based devices. However, it remains unclear how the inclusion of the bulky molecules into the pre-annealed, wet film influences the nucleation and subsequent crystallization of the perovskite film. Therefore, the exact mechanisms of both the efficiency- and stability-improvement need to be investigated in detail in order to be able to optimize these simplified approaches. For example, does the addition of the bulky molecule alter the formation of the 3D perovskite layer (and how) or simply passivate it after its formation? And does the (quasi-)2D layer still form solely at the surface of the 3D film or does the incorporation of the molecules into the wet film lead to passivation in the bulk of the 3D material as well?

Multimodal in situ characterization has been repeatedly shown to be an excellent tool to study nucleation and crystallization mechanisms and to provide a comprehensive understanding of film formation both of 3D perovskite films,[27–29] as well as of the formation of 2D/3D structures.[14,23] Recently, we used in situ grazing incidence wide angle X-ray scattering (GIWAXS) to investigate the structural changes induced by adding 2D passivation to the formation process of tin-based perovskites.[30] In the present study, we use in situ GIWAXS in combination with in situ optical characterization in order to provide a complete picture of the formation of the structural and opto-electronic properties of the more commonly-used lead-based perovskite films and how these are altered by adding bulky molecules to the antisolvent step. To do so, we use a simplified fabrication approach combining the modified 2D/3D fabrication process (Figure 1b) with the incorporation of large halides into the 2D/3D perovskite films, the integrated deposition and passivation strategy – exemplarily using PEACl as the organic molecule dissolved in isopropyl alcohol (IPA). Our approach consists of the deposition of the PEACl:IPA solution as the modified antisolvent (AS) during the 3D halide perovskite thin film fabrication thereby integrating the passivation via 2D perovskites into the deposition process of the 3D perovskite films. The major difference of this strategy is that the PEACl molecules are present during the crystallization of the perovskite films (here we use triple cation $Cs_{0.11}FA_{0.81}MA_{0.08}Pb(I_{0.87}Br_{0.13})_3$, where FA is formamidinium and MA is methylammonium), rather than being added post synthesis of the solid 3D film. We investigate the underlying changes in the crystallization pathways of the integrated films and show that this strategy effectively improves the nucleation and grain growth as well as the incorporation/intercalation of the PEACl into the 3D perovskite matrix. Comparing the nucleation and crystal growth using multimodal in situ characterization, we find that the incorporation of Cl in form of PEACl via the integrated deposition and passivation strategy stabilizes an intermediate solvate phase, retarding the growth of perovskite crystallites at room temperature. Subsequently, the integrated deposition and passivation strategy leads to larger average grain sizes and more homogeneous film morphology. This in turn improves the optoelectronic properties of the films and hence the performance and stability of resulting devices.

2. Results and Discussion

To investigate the effects of the integrated PEACl-drip on the formation dynamics of the perovskite thin films, we carried out several (multimodal) in situ experiments. **Figure 2** shows the evolution of the thin-films' optical and structural properties during spin coating and annealing as measured by in situ transmission (UV–vis, Figure 2a,e), PL (Figure 2b,f), and GIWAXS (Figure 2c,g). Figure 2a–d shows the respective results for a control sample without PEACl (but only IPA as AS) and Figure 2e–h for a sample using 3.0 mg mL^{-1} of PEACl in IPA as AS. Additional measurements of samples with varied PEACl content are shown in Figure S1, Supporting Information. Please note that the UV–vis measurements were taken in a N_2-fillled glove box, while the PL and GIWAXS measurements were taken using a N_2-flushed, multimodal spin coating and annealing setup at the Advanced Light Source (ALS). Details of the respective experimental procedures and method of aligning both time axes can be found in the Experimental Section.

Combining the results from these spectroscopic and diffraction measurements, we identify three growth stages in case of the control and four stages in the case of the PEACl-treated sample as indicated at the bottom of each panel in Figure 2. Stage I (prior to AS deposition) of the control sample shows a slight reduction of the position of the absorbance edge along with the absence of a PL signal and GIWAXS-peaks indicating the presence of a wet film that becomes slightly thinner during the spin coating.

Upon dripping of the AS (beginning of Stage II), we observe a continuous shift of the absorbance edge toward higher wavelengths (Figure 2a). The absorbance edge continues to shift until the end of the spin coating and seems to reach a steady state there before further shifting to the final position of the perovskite at the end of Stage II. We attribute this shift of the absorption edge to a combination of two factors. First, the absorption by an intermediate phase (see below) appears to shift the main absorption edge from ≈450 to 500 nm and second, first perovskite nuclei start absorbing in the range > 500 nm.

In good agreement with previous studies on $MAPbI_3$,[28,31] the AS-drip induces the emergence of a bright PL-signal that is considerably blue shifted compared to the bulk bandgap energy of the triple cation perovskite – here to about 1.84 eV compared to a final bulk bandgap energy of 1.64 eV. Following the argumentation in Ref. [28], we attribute this signal and its subsequent fast red shift to first quantum-confined nucleation and then growth of nano-crystallites. Upon heating, that is, at the end of Stage II, the PL signal diminishes due to temperature-induced quenching.

In situ GIWAXS shows the appearance of diffraction peaks at 0.47, 0.56, and 0.69 $Å^{-1}$ immediately after the AS-drop. These peaks are attributed to a solvate phase, presumably close to the MAI–PbI_2–DMF phase $(MA)_2Pb_3I_8{\cdot}2DMF$ with reported peaks at 0.46, 0.57, and 0.68 $Å^{-1}$.[32] Almost at the same time, we observe the nucleation of perovskite crystallites, that is, the appearance of a diffraction peak at 1.01 $Å^{-1}$, which can be attributed to the (100) diffraction peak of the cubic alpha phase perovskite[33,34] After its fast emergence, the intensity of the (100)-peak stays mostly unchanged during the remainder of the spin coating before it further increases during heating of the sample at the end of Stage

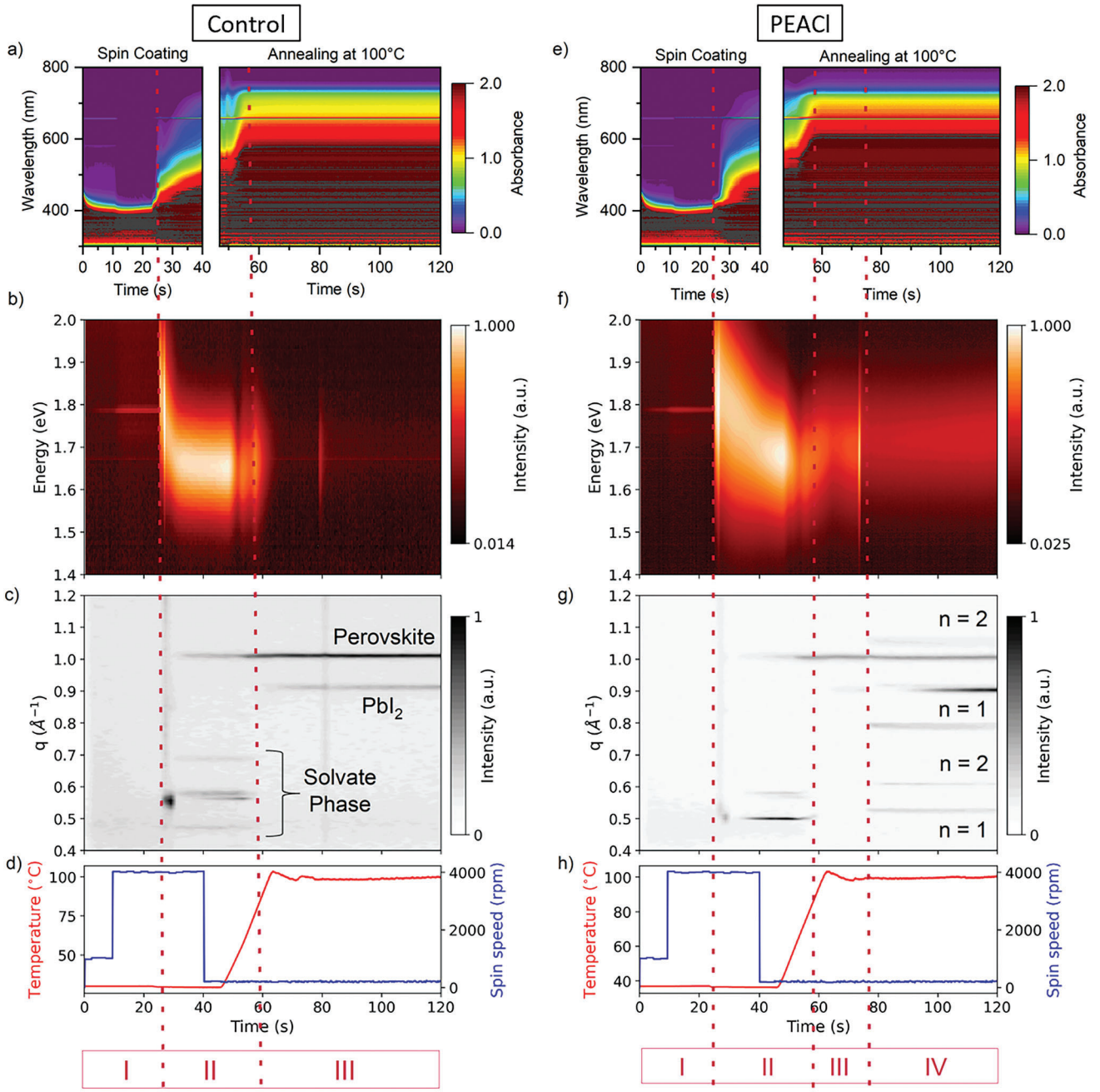

Figure 2. a,e) Time-correlated evolution of the absorbance, b,f) photoluminescence (PL)-emission, and c,g) GIWAXS during spin coating and annealing (d,h show spin speed and temperature curves) of perovskite films. The left column shows the film formation of a control sample, the right column shows the film formation of a sample treated with a mixed PEACl:IPA antisolvent with concentration of 3.0 mg mL^{-1}. Please note that the intensity on the PL-panels is plotted logarithmically and that the PL-emission of the 2D phases corresponding to PEACl is outside the range of our measurement setup (see Experimental Section for more details).

II (see Figure 2). Note that the additional peak observed at 0.58 $Å^{-1}$ could not be assigned to either the solvate or the perovskite phases.

The analysis of these complementary results suggests that the AS-dripping triggers the formation of $(MA)_2Pb_3I_8{\cdot}2DMF$ and simultaneously the nucleation of perovskite nanocrystals. While the growth of these nanocrystals is initially rapid as evidenced by the quick PL shift and initial appearance of the (100) perovskite peak in GIWAXS, further conversion to the perovskite phase is inhibited at room temperature due to the relative stability of the precursor-solvent complex.

After passing a critical temperature of about 80 °C (beginning of Stage III), the precursor-solvent phase disintegrates leading to its thermal decomposition and further solvent-evaporation, thus

further conversion to the perovskite phase as seen by the complete formation of the absorption edge of the perovskite in UV–vis. Indeed, this process is accompanied by an increase of the intensity of the (100) peak in GIWAXS. A few seconds into Stage III, an additional diffraction peak at 0.91 $Å^{-1}$ attributable to PbI_2 can be observed.

The case of the 2D-treated sample shows different dynamics and phase evolution compared to the control sample. In the following, we will first present a qualitative comparison with the control case, before we discuss an attempt to quantify the effects of the PEACl-treatment using samples with varying concentrations.

While the dynamics observed in Stage I follow the same pattern for the PEACl sample as for the control sample, the formation dynamics after the initial nucleation of the perovskite illustrated in Stage II occur much more slowly indicating a more gradual growth. After an initial redshift, the absorption edge reaches a plateau during the spin coating and does not further evolve until thermal activation. However, the absorption >500 nm appears slightly less strong than in case of the control, indicating weaker absorption by perovskite nuclei. During annealing, the final evolution of the perovskite absorption edge occurs more slowly for the sample prepared using AS with PEACl. In the PL spectra, we find a comparably bright emission right after dropping the AS at a similar position as in the case of the control sample without PEACl in it, however, the following redshift is significantly slower: it takes about 20 s as compared to 5 s in the control sample case. Diffraction measurements confirm the retarded growth, as the appearance of the (100)-diffraction peak after the AS with PEACl-drop is more gradual as compared to the control sample without PEACl in AS. Additionally, the diffraction peaks of the precursor-solvent phase are shifted indicating a decrease of the lattice parameter of the intermediate phase compared to $(MA)_2Pb_3I_8{\cdot}2DMF$ (peak positions for the PEACl sample are 0.50, 0.58, and 0.68 $Å^{-1}$). While the exact composition of this intermediate phase remains unclear, we speculate that the incorporation of the smaller halide Cl is responsible for the observed lattice distortion. Overall, there is strong evidence that the addition of PEACl to the AS retards the crystal growth at room temperature, in turn providing improved growth control.

Stage III begins similarly as compared to the control sample case, that is, with further growth of the perovskite crystallites and the segregation of PbI_2. However, shortly after reaching the maximum annealing temperature (Stage IV), the GIWAXS PbI_2-related peak vanishes for about 15 s before it re-appears. Interestingly, the PbI_2 signal changes from a diffuse and incomplete ring to a sharp arc indicating out-of-plane orientation (compare **Figure** 3a,b). Additionally, diffraction peaks emerge at 0.53, 0.61, 0.79, and 1.06 $Å^{-1}$. We attribute these peaks to the $n = 1$ and $n = 2$ phases of the layered 2D structures (see Figure 1b) suggesting the intercalation of the PEACl.[35,36] In Figure 3a,b, 2D GIWAXS frames taken at 120s after process begin, that is, during Stage IV, are displayed. These frames show that the peaks attributable to the $n = 1$ and $n = 2$ phases are strongly localized around the $q_x = 0$ plane indicating a strongly preferred orientation of the corresponding lattice planes parallel to the substrate. These plots indicate that the 2D molecules form 2D layers which exhibit strongly pronounced crystal orientation similar to the cases in which PEA-based molecules have been deposited after the formation of the 3D perovskite layer.[37] For traditionally deposited PEAI-layers, this has been explained by the fact that the (quasi-)2D layers preferably form at the surface of the perovskite film, exhibiting a strong preferential orientation parallel to the substrate.[24] Surprisingly, the GIWAXS data shown in Figure 3 suggest a similar orientation following the integrated deposition and passivation strategy. To investigate the depth distribution of the (quasi-) 2D layers in samples prepared by the integrated deposition and passivation strategy, we carried out X-ray photoelectron spectroscopy (XPS, Figure 3c,d) and time of flight secondary ion mass spectrometry (ToF-SIMS, Figure 3e and Figure S2, Supporting Information) investigations. In the N 1s XPS spectra, the PEACl addition to the antisolvent solution leads to the appearance of an additional peak at higher binding energy indicating the presence of a $C\text{-}NH_2$ species at the surface.[13] We attribute this additional contribution to the $C\text{-}NH_2$ group of PEA and its presence therefore as an indicator for the formation of the (quasi-)2D layers at the surface of the film. The presence of an additional layer at the surface is supported by the fact that the PEACl-containing films show a shift of the valence-band maximum (VBM) toward the Fermi level (VBM = 0.6 eV) as compared to the control (VBM = 1.15 eV) sample, which is in a good agreement with literature values for PEA-containing 2D/3D perovskite films.[38] Additionally, the SIMS depth profiles confirm the presence of PEA at the surface of the PEACl sample, and show that its signal remains under the detection limit for regions past about 8% of the film thickness indicating that most (if not all) PEACl-induced 2D-layers segregate to the surface of the film. Although the PEACl is dropped during the 3D perovskite film formation, the (quasi-)2D layer forms exclusively at the surface of the film indicating diffusion of the PEACl toward the surface – presumably during the annealing step since no 2D-related diffraction occurs before Phase IV.

Comparing the formation dynamics of samples prepared using various concentrations of PEACl in IPA (see Figure S1, Supporting Information), we find that the duration of the interruption of the PbI_2-signal is longer the higher the PEACl concentration. Therefore, we propose that the vanishing PbI_2-signal can be attributed to the consumption of PbI_2 during the reaction $2PbI_2 + PEACl \rightarrow (PEA)_2Pb(I,Cl)_4$ forming the $n = 1$ 2D-layer. As discussed above, this reaction only consumes part of the excess PbI_2, and the remaining lead iodide re-crystallizes after the formation of the 2D-layer, presumably in a layered structure. We speculate that the layered 2D matrix now acts as a seed-layer for layered growth of the PbI_2. Thereby, higher concentrations of PEACl can consume larger amounts of PbI_2 explaining the longer disappearance of the peak. This hypothesis is supported by the SIMS measurements in Figure 3e. They clearly show an accumulation of Pb at the very surface of the control sample indicating the presence of PbI_2 there, while no such accumulation is present at the surface of the sample prepared with PEACl in the AS. Interestingly, the $n = 2$ related peaks are not observed in the X-ray diffraction (XRD) patterns of the completed films (see **Figure** 4d). Tracking the evolution of these peaks for a longer period of time reveals that they slowly disappear during annealing (see Figure S3, Supporting Information). This behavior is in good agreement with a recent study in which we showed that during annealing of TC-perovskite/PEAI-films the $n > 1$ phases convert to the $n = 1$ phase

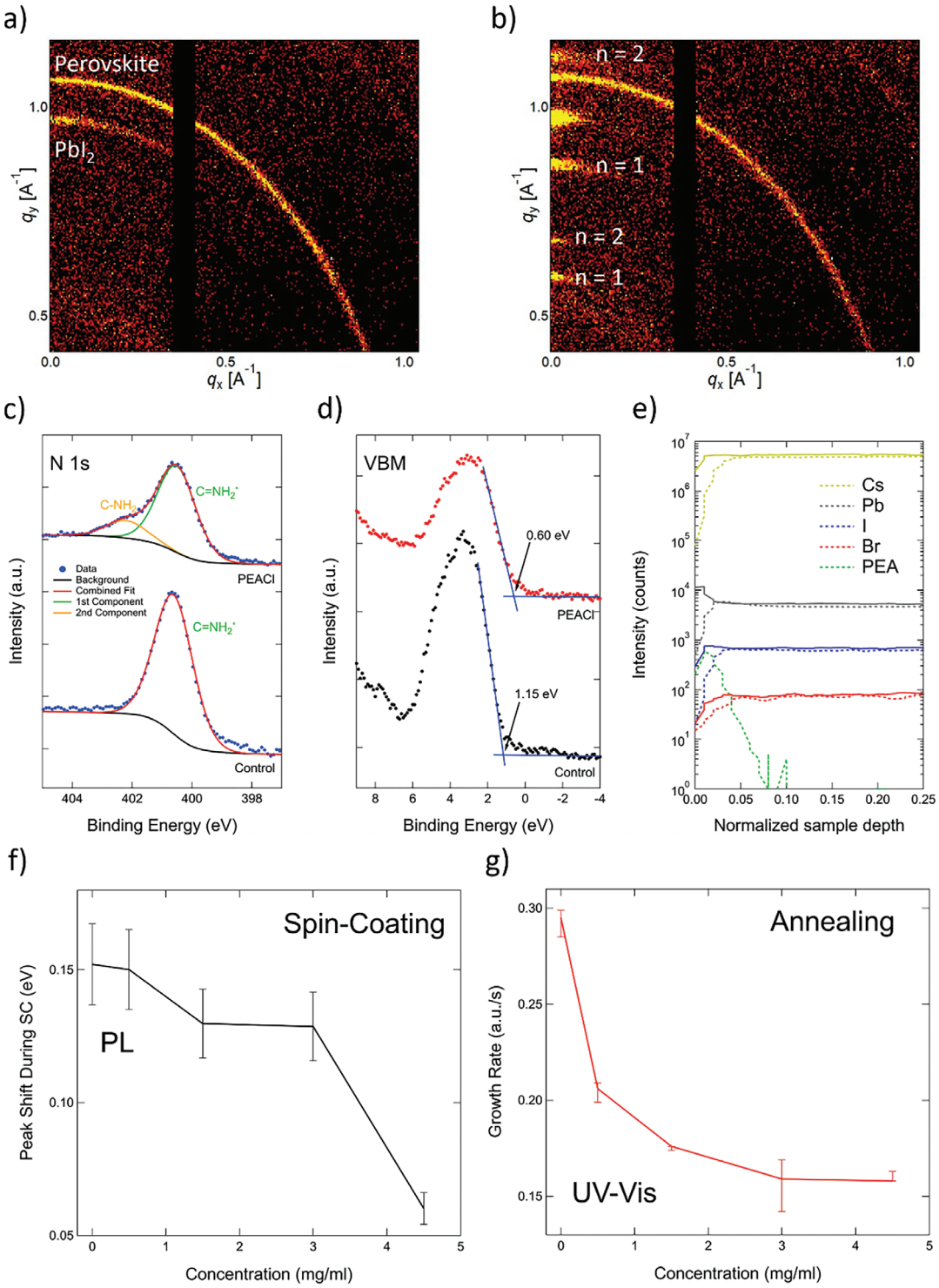

Figure 3. a) 2D-GIWAXS frames of the perovskite films prepared without (control) and b) with the PEACl in the AS samples taken at 120 s after process begin (intensity is given on a log scale). In the PEACl-treated sample, there are several, strongly oriented peaks attributable to the (quasi-) 2D phases. c,d) show the fitted XPS spectra of the N 1s and the valence band (valence band maximum) regions of the perovskite prepared without PEACl in the antisolvent solution (control) and with PEACl in the antisolvent solution. e) shows SIMS depth profiles for both samples – the control sample is represented by solid lines, the sample with PEACl in the AS by dashed lines. Here we only show the near-surface region of the sample, the full dataset can be found in Figure S2, Supporting Information. f) Shift of the PL peak position over time during the spin coating process (see Figure S4a, Supporting Information for PL data). g) Relative growth rates during annealing as extracted from UV–vis. See Figure S4, Supporting Information for details of the extraction of the growth rates. It can be clearly seen how a higher concentration of the PEACl steadily slows down the growth processes both during spin coating (PL) and annealing (UV–vis).

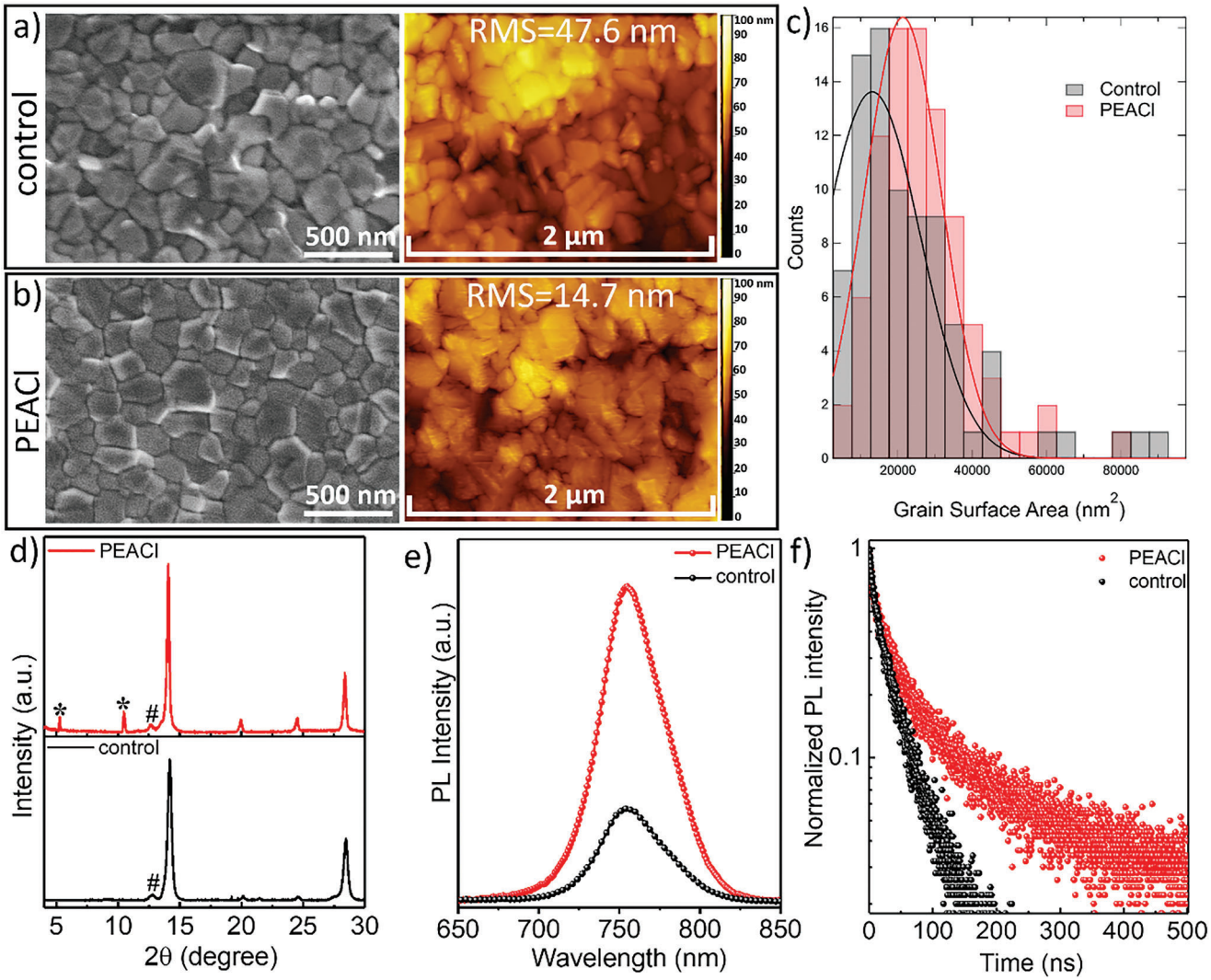

Figure 4. Ex situ characterization of PEACl-treated and control films. a,b) show top view scanning electron microscopy (SEM) images (left column), and atomic force microscopy (AFM) images (right column) of the control and the PEACl-treated film, respectively. c) shows the distributions of the grain sizes for each sample, d) XRD patterns (# is PbI_2, * is $n = 1$ phase), e) steady-state PL spectra, and f) time-resolved PL measurements of the films.

which seems to be more thermodynamically stable for these specific chemistries.[14]

In order to (semi-)quantify the slowing effect of PEACl on the crystal growth of the perovskite film, we extracted growth rates from the in situ measurements during spin coating and annealing for five different PEACl concentrations (Figure 3f,g). Due to the high PL quantum yield of perovskites, even small volume concentrations of perovskite embedded in amorphous precursor and/or solvate phase can be detected by PL whereas UV–vis and GIWAXS are not sensitive enough to detect a signal from the perovskite given the short acquisition time and signal to noise ratio.[28,29] Therefore, we used the magnitude of the PL-shift, that is, initial PL emission peak position minus bulk PL emission position, observed during the spin coating as an indicator of the growth rate of quantum-confined nuclei at room temperature. Figure 3g illustrates a decrease in growth rate with increasing PEACl concentration in AS as extracted from the evolution of the PL peak position during spin coating at room temperature.

After reaching a critical crystal size, this initial growth stagnates (see stabilizing behavior at the end of Stage II in Figure 2) and thermal activation is needed to continue the growth. We then used the slope of the increase of the absorption at 740 nm from UV–vis measurements as a measure for the thermally activated growth (see Figure 3g for the growth rates and Figure S4, Supporting Information for more details). The growth rates extracted from UV–vis show an exponential decrease with increasing PEACl-concentration in AS. Interestingly, Cl-derived perovskites from $PbCl_2$ have been reported in the past to crystallize much slower than acetate or other halide-derived perovskite films possibly due to relatively stable Cl-containing precursor phases and/or a competing mechanism of MACl-formation and -evaporation.[39,40] Accordingly, we propose that the incorporation of Cl significantly stabilizes the intermediate phase requiring thermal energy to dissociate it and therefore slowing down the perovskite growth. In order to test whether the PEA^+ ions contribute to the retarding effect on the perovskite crystallization,

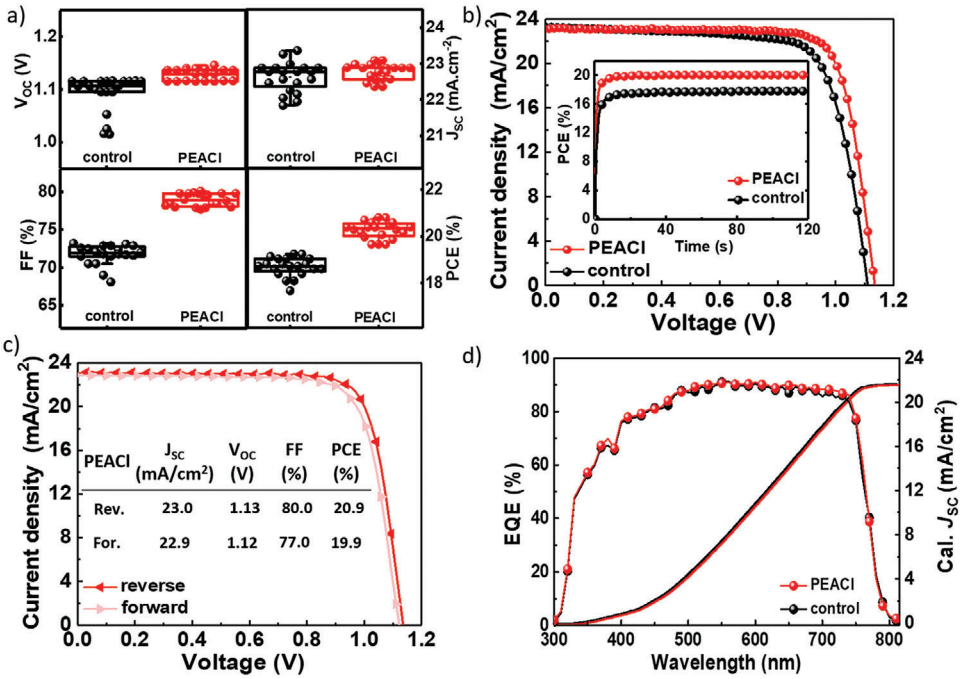

Figure 5. a) Photovoltaic parameters of devices based on the PEACl-treated and control films as well as b) current density – voltage (*J–V*) curves of the best devices each and their stabilized *PCE* (inset in b). c) shows the reverse and forward *J–V* curve of the best device with PEACl-treatment. d) The external quantum efficiency of champion devices and their corresponding calculated J_{SC}.

we compared the evolution of the PL signal during spin-coating for a control sample and a sample with 3.0 mg mL^{-1} of PEAI (phenethyl ammonium iodide) in the anti-solvent. As shown in Figure S5, Supporting Information, there is a much less pronounced delay in the nucleation/crystallization visible in case of the PEAI. We therefore conclude that it is very likely that the Cl is the main cause for the delay in perovskite formation similar to the argumentation in Ref. [39].

In a next step, we carried out additional ex situ thin film and device characterizations. **Figure 4** shows a comparison of the morphology, roughness, structure, and optoelectronic properties of thin films with and without the PEACl in AS. Addition of PEACl to AS leads to smoother (RMS roughness of 14.7 nm vs 47.6 nm) and more homogeneous films (Figure 4a,b). The SEM images as well as a quantitative comparison of the grain size distribution derived from the images (Figure 4c) reveal slightly more homogeneous and larger grain sizes for samples containing PEACl in AS. Furthermore, we observe a strongly increased steady state PL intensity (Figure 4e) and a longer carrier lifetime (time-resolved PL measurements in Figure 4f, $\tau_{Control}$ = 29.3 ns and τ_{PEACl} = 80.4 ns) for the samples prepared with PEACl in AS. Taking into account the slower crystal growth in the presence of PEACl in AS as discussed above, we propose that this slower crystallization is more controlled leading to more homogeneous grain growth.[41,42] This in turn reduces the density of grain boundaries in the film and subsequently the defect-assisted non-radiative recombination rate in the bulk of the film, increasing the charge carrier lifetime. Although defect-assisted recombination at the grain boundaries is not necessarily considered as the main recombination mechanism in perovskite-based solar cells, it does contribute to limited device efficiency and stability.[43,44] Additionally, the presence of PEACl may directly passivate defects at the surface.[22]

To better understand the film quality's effect on the photovoltaic performance, we fabricated solar cells using perovskite films with and without PEACl in the AS. **Figure 5a** illustrates the statistical data of the photovoltaic parameters of PEACl- and control-PSCs. The PEACl-PSCs show significantly improved device performance and reproducibility compared to the control-PSCs. The control-PSCs show an average *PCE* of (18.69 ± 0.39) %, with an average J_{SC} = (22.62 ± 0.40) mA cm^{-2}, V_{OC} = (1.09 ± 0.03) V, and *FF* = (71.73 ± 1.30) %. Remarkably, for the PEACl perovskite films the average *PCE* increases to (20.26 ± 0.32) %, with an average J_{SC} = (22.77 ± 0.21) mA cm^{-2}, V_{OC} = (1.12 ± 0.01) V, and *FF* = (78.96 ± 0.82) %. These performance improvements in PEACl perovskite films can be mainly explained by reduction of the non-radiative recombination rate (Figure 4e,f) and improvement of the interface of perovskite/HTL due to lower surface roughness (Figure 4a–c). Figure 5b compares the current–voltage (*J–V*) curves of the champion devices of the control and the PEACl batches, respectively. The champion PEACl-PSC showed a V_{OC} of 1.13 V, a J_{SC} of 23.0 mA cm^{-2} and an *FF* of 80.0%, which resulted in a *PCE* of 20.9%, remarkably higher than that (*PCE* = 19.0%) of the control-PSC (V_{OC} = 1.10 V, J_{SC} = 23.2 mA cm^{-2}, and *FF* = 73.2%). To verify the performance of the champion devices under real device operation conditions, the maximum power point (MPP) was measured under continuous illumination at 25 °C for 2 min (inset in Figure 5b). The PEACl- and control-PSCs showed stabilized *PCE* of ≈20% and ≈17%, respectively. To explore the reason for low *PCE* deficient (*PCE* of *J–V* measurement- stabilized *PCE*) of PEACl-PSCs (≈1%), we measured the *J–V* hysteresis. As shown in Figure 5c, the

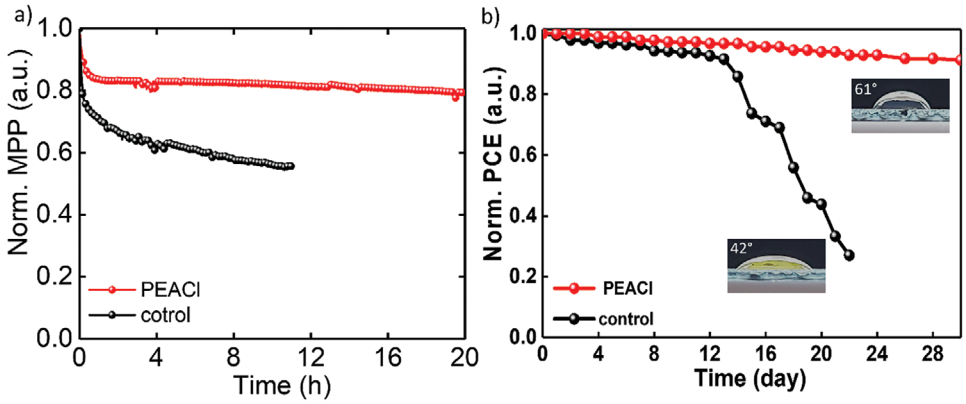

Figure 6. a) Stabilized power output at the maximum power point voltage over time under continuous illumination at 25 °C, data normalized to the initial value. b) Long term stability at 60% relative humidity in dark at 25 °C. Insets show contact angle measurements for each sample (42° for the control and 61° for the PEACl-sample).

photovoltaic parameters do not change under different *J–V* direction measurements, which is likely due to the overall reduced bulk defect density and suppressed recombination during PEACl-PSC operation with better film quality and therefore confirming the achieved high stabilized *PCE* for this device.[45–47] To confirm the accuracy of our *J–V* measurement, we also measured the external quantum efficiency (*EQE*) of the champion PEACl- and control PSCs and used that data to calculate its J_{SC} values. As shown in Figure 5d, both devices showed a homogeneous light response in the whole UV–vis light range with calculated J_{SC} values of ≈21.7 mA cm^{-2} in both cases, which is in good agreement with the values achieved from the corresponding *J–V* curves (with an acceptable error of 5%).[48,49]

To finally assess whether the integrated deposition and passivation strategy improves the stability of the perovskite-based devices under operating and humid conditions (60% RH), we conducted stability tests (see **Figure 6**). Figure 6a shows the evolution of the device performance at its MPP under continuous illumination at 25 °C and Figure 6b shows the normalized *PCE* during storage of the devices at 60% relative humidity in dark at 25 °C. The surface of the PEACl-treated samples is significantly more hydrophobic, see inset of Figure 6b contributing to the significantly improved stability compared to the untreated control.

3. Conclusions

We propose that the introduction of Cl via bulky cations during the formation of metal halide perovskite films slows down the crystal growth, subsequently leading to larger grains, more homogeneous grain size distribution, smoother films with fewer pinholes, and improved charge carrier lifetime. These improvements reduce the carrier recombination at grain boundaries and significantly enhance the device's *FF* by >5% (absolute). We suggest that the Cl is incorporated into a long-lived precursor-solvate phase, slowing down the precursor conversion to perovskite. During annealing of the film, the PEACl diffuses to the surface of the film, forming hydrophobic (quasi-)2D structures that improve the stability of the devices and may additionally passivate surface defects. An integrated deposition and passivation strategy using PEACl in AS was presented to control the growth of halide perovskites and improve their performance and stability while reducing process complexity.

4. Experimental Section

Materials: *N,N*-dimethylformamide (DMF, 99.8%), dimethylsulfoxide (DMSO, 99.9%), Spiro-OMeTAD, 4-tert-butylpyridine (TBP), chlorobenzene (CB), and lithium bis (trifluoromethylsulfonyl) imide salt (Li-TFSI), Cesium iodide (CsI, 99.9%) were purchased from Sigma Aldrich Co., Ltd. Lead (II) iodide (PbI_2, 99.999%), Lead (II) bromide ($PbBr_2$, 99.999%) were purchased from TCI Chemicals. Formamidinium iodide (FAI, 99.9%), and methylammonium bromide (MABr, 99.9%) were purchased from GreatCell Solars. SnO_2 colloid precursor (tin (IV) oxide, 15% in H_2O colloidal dispersion) was purchased from Alfa Aesar. All salts and solvents were used as received without any further purifications.

Device Fabrication: The pre-patterned ITO-on-glass substrates (sheet resistance 15 Ω sq^{-1}, Luminescence Technology) were cleaned consecutively with deionized (DI) water, acetone, and isopropyl alcohol (IPA, Sigma-Aldrich) in an ultrasonic bath for 10 min, followed by UV-O_3 treatment for 30 min. In the next step, a thin layer of 2.04 wt% colloidal SnO_2 nanoparticles was spin-coated onto the ITO substrates (4000 rpm for 30 s) as electron transport layer (ETL), followed by an annealing step at 150 °C for 30 min.

The ETL substrates were transferred into a nitrogen atmosphere glove box for the deposition of the perovskite films. The triple cation perovskite ($Cs_{0.05}(MA_{0.17}FA_{0.83})_{0.95}Pb(I_{0.83}Br_{0.17})$) precursor solution was prepared from a precursor solution containing FAI (1 M), PbI_2 (1.1 M), MABr (0.2 M), $PbBr_2$ (0.2 M), and CsI (1.5 M). The perovskite solution was spin-coated using a two-step program at 1000 and 4000 rpm for 10 and 30 s, respectively. In our method, during the second step IPA containing different concentrations of phenethylammonium chloride (PEACl) were poured on the spinning substrate 5 s prior to the end of the program. Spiro-MeOTAD solution (83.32 mg mL^{-1} in CB) with addition of Li-TFSI in acetonitrile (0.18 M) and tBP (1 mL in 9 mL CB) were spin-coated onto the films at 5000 rpm for 1 min, and oxidized for 24 h. Finally, a gold electrode (100 nm) was vacuum-deposited at the pressure of ≈10^{-7} torr.

Multimodal In Situ PL and GIWAXS Measurements: The PL and GIWAXS data were collected at the 12.3.2 microdiffraction beamline of the Advanced Light Source (ALS) in a custom-made analytical chamber, allowing for processing of the thin film and simultaneous multimodal in situ measurements.[28] The pre-patterned ITO-on-glass substrates were purchased from MSE Supplies and consecutively cleaned in an ultrasonic bath. Prior to thin film fabrication, each substrate was plasma cleaned for 5 min, placed onto the integrated spin coating puck-heater, and secured

in place by a heat transfer paste. 50 µL of a liquid precursor prepared by dissolving 507 mg PbI_2, 73 mg $PbBr_2$, 172 mg FAI, and 22.5 mg MABr in a 1 mL solvent mixture of 4:1 DMF:DMSO and adding 89 µL CsI solution (comprised of 39 mg CsI in 100 µL DMSO) was pipetted and deposited onto the surface of the substrate and the chamber was sealed off from the external environment and held under a constant nitrogen flow. The deposition of the 2D material was combined with the antisolvent (AS) drop in lieu of the typical two-step process in which the 3D perovskite layer is completed prior to deposition of the 2D material to reduce both the processing time and the complexity of the deposition process. The spin coating recipe consists of a two-step process, first 10s at 1000 rpm and then 30s at 4000 rpm. 15s into the second spin coating step ($t = 25$ s), a stream of antisolvent (IPA containing prescribed concentrations of phenethylammonium chloride (PEACl)) was dispensed through a remotely controlled pipette. At the end of the spin coating protocol, the spin speed was reduced to 200 rpm to ensure uniform measurement conditions during the following annealing step. For that, a heating protocol was remotely initiated, in two stages. In the first stage ($t = 46$–63 s), the temperature was increased linearly at a rate of 4.1 °C s^{-1} until it reached 100 °C and stabilized. Thereafter, the temperature was maintained at 100 °C until the end of the experiment ($t = 63$–1023 s). The temperature of the heating puck was recorded by a pre-calibrated Raytek MI3 pyrometer, which regulated the annealing temperature and protocol through a pre-programmed PID loop.

During both spin coating and annealing PL and GIWAXS data were continuously recorded. The incident angle of the incoming X-ray beam was set to 1° with a beam energy of 10 keV. The sample detector distance (SDD) was ≈155 mm and the detector was positioned at an angle of 35° from the sample plane. The GIWAXS data were recorded with an integration time of one second using a Pilatus 1 M 2D detector (Dectris Ltd.). Photoluminescence excitation was achieved through a 405 nm Thorlabs diode-pumped solid-state laser with a power density at the substrate of about 5 mW cm^{-2}. The resultant photoluminescence signal was collected by a lens and focused on an optical fiber guiding it to a grating OceanOptics QE Pro spectrometer for detection. Note that the GIWAXS and PL measurements were initiated simultaneously, such that the resultant data were time-correlated. In order to obtain the plots of q versus time in Figure 2, the measured GIWAXS frames were calibrated using an Al_2O_3 reference sample and each frame was integrated along the χ-axis from $\chi = -70°$ to $\chi = 70°$. No significant preferential orientation was measured for the 3D perovskites. Data evaluation was done using software written in house.

UV–vis Characterization: The UV–vis absorbance spectra of the perovskite films were measured during both spin coating and annealing using a self-built setup in a nitrogen filled glovebox.[50] A hot plate was used to anneal the films at the desired temperature of 100 °C. For the in situ absorbance measurements, an Ocean Optics spectrometer (Flame) coupled with fibre optics was used to acquire the transmission data with a wavelength spacing of about 0.2 nm and an integration time of 0.02 s, averaging over 10 scans, for the spin coating measurements and an integration time of 0.006 s, averaging over 15 scans, for the annealing measurements. The equation $A\lambda = -\log_{10}(T\lambda)$ was used to calculate the UV–vis absorption spectra from the transmission spectra, where $A\lambda$ is the absorbance at a certain wavelength (λ), and $T\lambda$ is the corresponding transmitted radiation. The in situ UV–vis transmission/absorption measurements were obtained using an identical set-up to that outlined in the previous work.[50] To enable temporal comparison between these data and those obtained from the PL/GIWAXS measurements, a common time axis was generated using the temperature and spin speed log files from the beamline. To this end, the beginning of the UV–vis annealing data was aligned with the initiation of the linear heating step at the beamline at $t = 46$ s, and the end of the spin coating UV–vis data was correlated with the reduction of the spin speed to 200 rpm at $t = 40$ s.

SEM: The field emission SEM from HITACHI was used to characterize the morphologies of the films with an accelerating voltage of 3 kV.

AFM: The atomic force microscope (AFM, Dimension 3100 + Nanoscope V 7.0, VEECO) was operated in tapping mode to acquire the images of the surfaces of perovskite films.

XRD: The thin film crystallinity was measured using an X-ray Diffraction (SmartLab SE from Rigaku) machine with a HyPix-400 (2D HPAD) detector.

SSPL and TRPL: Steady-state photoluminescence (SSPL) measurements were conducted using a room temperature solid-state photoluminescence (RTPL), FluoroMax Plus HORIBA Scientific. Time-resolved photoluminescence (TRPL) measurements were performed using a pulsed laser source with a wavelength of 474 nm and a fluence of ≈400 nJ cm^{-2}. The samples were excited from the glass side under ambient conditions.

J–V: The *J–V* characteristics of the solar cells were recorded in the ambient atmosphere under AM 1.5 G, 100 mW cm^{-2} spectrum (WAVELABS, SINUS-70) using a Keithley 2400 source meter. The solar cells were unencapsulated during the test and measured in both forward and reverse directions from −0.2 to 1.3 V with 50 mV s^{-1}. The maximum power point (MPP) was tracked by using a perturband-observe method. The temperature of the solar cells set to 25 °C by an actively controlled Peltier element during *J–V* analyses and MPP tracking.

XPS: The X-ray photoelectron spectroscopy measurements were done using a Specs GmbH system with a non-monochromatic Al-Kα source with a photon energy of 1486.6 eV. The samples were measured in dark under a pressure of 10^{-9} mbar without use of any charge neutralizer. The photoemitted electrons were collected by an hemispherical analyzer (Omicron) at an angle of 90° to the surface of the sample using a pass energy of $E_{pass} = 20$ eV. The core level spectra were corrected using the C1s spectra.

ToF-SIMS: The ToF-SIMS5 from Iontof used a 30 keV Bi liquid metal ion gun for generating the secondary ions. A time of flight mass detector recorded ions, molecules and cluster up to 1000 amu in a mass resolution of 4000 units per mass unit. A second ion gun was necessary to enhance the sputter rate for depth profiling. A 10 keV oxygen gas cluster ion gun was chosen to prevent the fracture of large organic molecules. The detection area had a size of 50 × 50 µm^2 and the sputter area of 400 × 400 µm^2 for the blanking of the crater edge. The following ions and clusters were selected for the depth profile $C_6H_6^+$ (PEA), Cs^+, Pb^+, Cs_2Br^+, and Cs_2I^+. Depth axes were normalized for a better comparison.

Supporting Information

Supporting Information is available from the Wiley Online Library or from the author.

Acknowledgements

T.K. acknowledges funding by the German Research Foundation (DFG) under fellowship number KO6414. T.K. acknowledges support by the U.S. Department of Energy (DOE), Office of Science, Office of Basic Energy Sciences, Materials Sciences and Engineering Division under Contract No. DE-AC02-05-CH11231 (D2S2 program KCD2S2). M.G. acknowledges summer research funding from University of California, Berkeley and Lawrence Berkeley National Laboratory. M.S. and R.R. acknowledges funding by ProperPhotoMile. Project ProperPhotoMile is supported under the umbrella of SOLARERA.NET Co-funded by The Spanish Ministry of Science and Education and the AEI under the project PCI2020-112185 and CDTI project number IDI-20210171; the Federal Ministry for Economic Affairs and Energy on the basis of a decision by the German Bundestag project number FKZ 03EE1070B and FKZ 03EE1070A and the Israel Ministry of Energy with project number 220-11-031. M.S. thanks the German Research Foundation (DFG) for funding (SPP2196, 431314977/GRK 2642). M.S., M.M.B. and C.D. thank Helmholtz Young Investigator Group FRONTRUNNER. M.S. acknowledges funding from the European Research Council under the Horizon Europe programme (LOCAL-HEAT, grant agreement no. 101041809). M.S. acknowledges funding from the German Bundesministerium für Bildung and Forschung (BMBF), project "NETPEC" (01LS2103E). M.K. and J.I.F acknowledge funding from the Zentrales Innovationsprogramm Mittelstand (ZIM), Federal Ministry of Economics and Climate Protection under project number KK5087602BR1. Part of the work was carried out as a user project at the Molecular Foundry,

a user facility supported by the Office of Science, Office of Basic Energy Sciences, of the U.S. Department of Energy under Contract No. DE-AC02–05CH11231. Work at the Advanced Light Source (ALS) was done at beamline 12.3.2. The ALS is a DOE Office of Science User Facility under contract no. DE-AC02-05CH11231. The authors thank Jonathan Slack for his tremendous efforts developing the multimodal spin coater used at the beamline.

Open access funding enabled and organized by Projekt DEAL.

Conflict of Interest

The authors declare no conflict of interest.

Data Availability Statement

The data that support the findings of this study are available from the corresponding author upon reasonable request.

Keywords

2D/3D perovskites, crystallization, in situ characterization, stability

Received: September 6, 2023
Revised: February 5, 2024
Published online:

[1] T. Wu, Z. Qin, Y. Wang, Y. Wu, W. Chen, S. Zhang, M. Cai, S. Dai, J. Zhang, J. Liu, Z. Zhou, X. Liu, H. Segawa, H. Tan, Q. Tang, J. Fang, Y. Li, L. Ding, Z. Ning, Y. Qi, Y. Zhang, L. Han, *Nano-Micro Lett.* **2021**, *13*, 152.
[2] R. Sharma, A. Sharma, S. Agarwal, M. S. Dhaka, *Sol. Energy* **2022**, *244*, 516.
[3] H. Lu, A. Krishna, S. M. Zakeeruddin, M. Grätzel, A. Hagfeldt, *iScience* **2020**, *23*, 101359.
[4] K. O. Ogunniran, N. T. Martins, *IOP Conf. Ser.: Earth Environ. Sci.* **2021**, *655*, 012049.
[5] C. Das, M. Kot, T. Hellmann, C. Wittich, E. Mankel, I. Zimmermann, D. Schmeisser, M. Khaja Nazeeruddin, W. Jaegermann, *Cell Rep. Phys. Sci.* **2020**, *1*, 100112.
[6] M. Kot, L. Kegelmann, C. Das, P. Kus, N. Tsud, I. Matolinova, S. Albrecht, V. Matolin, D. Schmeisser, *ChemSusChem* **2018**, *11*, 3640.
[7] I. Kafedjiska, G. A. Farias-Basulto, P. Reyes-Figueroa, T. Bertram, A. Al-Ashouri, C. A. Kaufmann, R. Wenisch, S. Albrecht, R. Schlatmann, I. Lauermann, *Sol. Energy Mater. Sol. Cells* **2023**, *254*, 112248.
[8] I. Kafedjiska, G. Farias Basulto, F. Ruske, N. Maticiuc, T. Bertram, C. A. Kaufmann, R. Schlatmann, I. Lauermann, *J. Phys. Energy* **2023**, *5*, 024014.
[9] D.-K. Lee, N.-G. Park, *Appl. Phys. Rev.* **2023**, *10*, 011308.
[10] S. Liu, Y. Guan, Y. Sheng, Y. Hu, Y. Rong, A. Mei, H. Han, *Adv. Energy Mater.* **2020**, *10*, 1902492.
[11] R. K. Raman, S. A. G. Thangavelu, S. Venkataraj, A. Krishnamoorthy, *Renewable Sustainable Energy Rev.* **2021**, *151*, 111608.
[12] L. Xiang, F. Gao, Y. Cao, D. Li, Q. Liu, H. Liu, S. Li, *Org. Electron.* **2022**, *106*, 106515.
[13] C. A. R. Perini, E. Rojas-Gatjens, M. Ravello, A.-F. Castro-Mendez, J. Hidalgo, Y. An, S. Kim, B. Lai, R. Li, C. Silva-Acuña, J.-P. Correa-Baena, *Adv. Mater.* **2022**, *34*, 2204726.
[14] T. Kodalle, R. F. Moral, L. Scalon, R. Szostak, M. Abdelsamie, P. E. Marchezi, A. F. Nogueira, C. M. Sutter-Fella, *Adv. Energy Mater. 13*, 2201490.
[15] A. H. Proppe, A. Johnston, S. Teale, A. Mahata, R. Quintero-Bermudez, E. H. Jung, L. Grater, T. Cui, T. Filleter, C.-Y. Kim, S. O. Kelley, F. De Angelis, E. H. Sargent, *Nat. Commun.* **2021**, *12*, 3472.
[16] Y.-W. Jang, S. Lee, K. M. Yeom, K. Jeong, K. Choi, M. Choi, J. H. Noh, *Nat. Energy* **2021**, *6*, 63.
[17] G. Grancini, M. K. Nazeeruddin, *Nat. Rev. Mater.* **2019**, *4*, 4.
[18] A. A. Sutanto, P. Caprioglio, N. Drigo, Y. J. Hofstetter, I. Garcia-Benito, V. I. E. Queloz, D. Neher, M. K. Nazeeruddin, M. Stolterfoht, Y. Vaynzof, G. Grancini, *Chemistry* **2021**, *7*, 1903.
[19] X. Liu, T. Webb, L. Dai, K. Ji, J. A. Smith, R. C. Kilbride, M. Yavari, J. Bi, A. Ren, Y. Huang, Z. Wang, Y. Shen, G. Shao, S. J. Sweeney, S. Hinder, H. Li, D. G. Lidzey, S. D. Stranks, N. C. Greenham, S. R. P. Silva, W. Zhang, *Energy Environ. Mater.* **2022**, *5*, 670.
[20] G.-W. Kim, A. Petrozza, *Adv. Energy Mater.* **2020**, *10*, 2001959.
[21] H.-S. Yoo, N.-G. Park, *Sol. Energy Mater. Sol. Cells* **2018**, *179*, 57.
[22] Q. Jiang, Y. Zhao, X. Zhang, X. Yang, Y. Chen, Z. Chu, Q. Ye, X. Li, Z. Yin, J. You, *Nat. Photonics* **2019**, *13*, 460.
[23] C. A. R. Perini, A.-F. Castro-Mendez, T. Kodalle, M. Ravello, J. Hidalgo, M. Gomez-Dominguez, R. Li, M. Taddei, R. Giridharagopal, J. Pothoof, C. M. Sutter-Fella, D. S. Ginger, J.-P. Correa-Baena, *ACS Energy Lett.* **2023**, *8*, 1408.
[24] R. Azmi, E. Ugur, A. Seitkhan, F. Aljamaan, A. S. Subbiah, J. Liu, G. T. Harrison, M. I. Nugraha, M. K. Eswaran, M. Babics, Y. Chen, F. Xu, T. G. Allen, A. U. Rehman, C.-L. Wang, T. D. Anthopoulos, U. Schwingenschlogl, M. De Bastiani, E. Aydin, S. De Wolf, *Science* **2022**, *376*, 73.
[25] F. Wang, J. Du, Y. Zhang, M. Yang, D. Han, L. Yang, L. Fan, Y. Sui, Y. Sun, J. Yang, *J. Mater. Sci. Technol.* **2021**, *92*, 21.
[26] D.-H. Kang, S.-Y. Kim, J.-W. Lee, N.-G. Park, *J. Mater. Chem. A* **2021**, *9*, 3441.
[27] S.-G. Kim, J.-H. Kim, P. Ramming, Y. Zhong, K. Schötz, S. J. Kwon, S. Huettner, F. Panzer, N.-G. Park, *Nat. Commun.* **2021**, *12*, 1554.
[28] S. Pratap, F. Babbe, N. S. Barchi, Z. Yuan, T. Luong, Z. Haber, T.-B. Song, J. L. Slack, C. V. Stan, N. Tamura, C. M. Sutter-Fella, P. Müller-Buschbaum, *Nat. Commun.* **2021**, *12*, 5624.
[29] F. Babbe, C. M. Sutter-Fella, *Adv. Energy Mater.* **2020**, *10*, 1903587.
[30] F. Yang, R. Zhu, Z. Zhang, Z. Su, W. Zuo, B. He, M. H. Aldamasy, Y. Jia, G. Li, X. Gao, Z. Li, M. Saliba, A. Abate, M. Li, *Adv. Mater. 36*, 2308655.
[31] W. Zuo, M. M. Byranvand, T. Kodalle, M. Zohdi, J. Lim, B. Carlsen, T. Magorian Friedlmeier, M. Kot, C. Das, J. I. Flege, W. Zong, A. Abate, C. M. Sutter-Fella, M. Li, M. Saliba, *Adv. Mater.* **2023**, *35*, 2302889.
[32] A. A. Petrov, I. P. Sokolova, N. A. Belich, G. S. Peters, P. V. Dorovatovskii, Y. V. Zubavichus, V. N. Khrustalev, A. V. Petrov, M. Grätzel, E. A. Goodilin, A. B. Tarasov, *J. Phys. Chem. C* **2017**, *121*, 20739.
[33] M. Qin, K. Tse, T.-K. Lau, Y. Li, C.-J. Su, G. Yang, J. Chen, J. Zhu, U.-S. Jeng, G. Li, H. Chen, X. Lu, *Adv. Mater.* **2019**, *31*, 1901284.
[34] M. Abdelsamie, J. Xu, K. Bruening, C. J. Tassone, H.-G. Steinrück, M. F. Toney, *Adv. Funct. Mater.* **2020**, *30*, 2001752.
[35] P. Cai, Y. Huang, H. J. Seo, *J. Phys. Chem. Lett.* **2019**, *10*, 4095.
[36] M. Rahil, R. M. Ansari, C. Prakash, S. S. Islam, A. Dixit, S. Ahmad, *Sci. Rep.* **2022**, *12*, 2176.
[37] M. E. F. Bouduban, V. I. E. Queloz, V. M. Caselli, K. T. Cho, A. R. Kirmani, S. Paek, C. Roldan-Carmona, L. J. Richter, J. E. Moser, T. J. Savenije, M. K. Nazeeruddin, G. Grancini, *J. Phys. Chem. Lett.* **2019**, *10*, 5713.
[38] M. Lee, E. Choi, A. M. Soufiani, J. Lim, M. Kim, D. Chen, M. A. Green, J. Seidel, S. Lim, J. Kim, X. Dai, R. Lee-Chin, B. Zheng, Z. Hameiri, J. Park, X. Hao, J. S. Yun, *Adv. Funct. Mater.* **2021**, *31*, 2008908.
[39] T.-B. Song, Z. Yuan, M. Mori, F. Motiwala, G. Segev, E. Masquelier, C. V. Stan, J. L. Slack, N. Tamura, C. M. Sutter-Fella, *Adv. Funct. Mater.* **2020**, *30*, 1908337.

[40] K. H. Stone, A. Gold-Parker, V. L. Pool, E. L. Unger, A. R. Bowring, M. D. McGehee, M. F. Toney, C. J. Tassone, *Nat. Commun.* **2018**, *9*, 3458.
[41] C. W. Lan, W. C. Lan, T. F. Lee, A. Yu, Y. M. Yang, W. C. Hsu, B. Hsu, A. Yang, *J. Cryst. Growth* **2012**, *360*, 68.
[42] B. Ding, Y. Li, S.-Y. Huang, Q.-Q. Chu, C.-X. Li, C.-J. Li, G.-J. Yang, *J. Mater. Chem. A* **2017**, *5*, 6840.
[43] T. S. Sherkar, C. Momblona, L. Gil-Escrig, J. Ávila, M. Sessolo, H. J. Bolink, L. J. A. Koster, *ACS Energy Lett.* **2017**, *2*, 1214.
[44] A.-F. Castro-Méndez, J. Hidalgo, J.-P. Correa-Baena, *Adv. Energy Mater.* **2019**, *9*, 1901489.
[45] S. Meloni, T. Moehl, W. Tress, M. Franckevicius, M. Saliba, Y. H. Lee, P. Gao, M. K. Nazeeruddin, S. M. Zakeeruddin, U. Rothlisberger, M. Graetzel, *Nat. Commun.* **2016**, *7*, 10334.
[46] W. Tress, N. Marinova, T. Moehl, S. M. Zakeeruddin, M. K. Nazeeruddin, M. Grätzel, *Energy Environ. Sci.* **2015**, *8*, 995.
[47] W. Tang, Y. Chen, J. Yang, R. Yuan, Y. Lv, Q. Ma, Y. Wu, P. Zhang, W.-H. Zhang, *J. Power Sources* **2021**, *482*, 228965.
[48] M. Saliba, L. Etgar, *ACS Energy Lett.* **2020**, *5*, 2886.
[49] M. Saliba, E. Unger, L. Etgar, J. Luo, T. J. Jacobsson, *Nat. Commun.* **2023**, *14*, 5445.
[50] C. M. Sutter-Fella, *Adv. Energy Mater.* **2021**, *11*, 2003534.